

Chapter 2

Study on Forward Transient Time Distribution and Cutoff Frequency for HBT Devices

2.0 Original Physics

In this section, a new-developed transit time estimation methodology based on the calibrated SIMS profiles of the doping species in fabricating modern SiGe HBT devices were described and demonstrated. Such new approach could decouple the components which consisting the transit time of the devices. As a result, the detail compositions of the device transit time could be studied physically and these knowledge and research methodology could benefit the device development in next generation.

First, the composition of the device transit time τ_{total} should be identified based on the derivation results:

$$\tau_{total} = \tau_F + \tau_J + \tau_{RC} \quad (2.0.1)$$

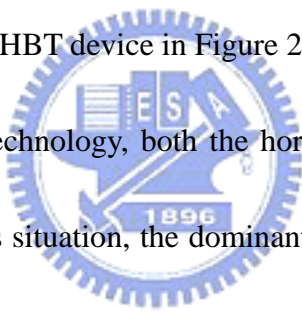
$$\tau_F = \tau_B + \tau_E + \tau_C \quad (2.0.2)$$

$$\tau_J = \frac{V_T}{I_C} (C_{BE} + C_{BC}) \quad (2.0.3)$$

$$\tau_{RC} = (r_C + r_E) C_{BC} \quad (2.0.4)$$

Eq. 2.0.1 to Eq. 2.0.4 were derived based on the high frequency small signal model

illustrated in Figure 2.0.1 with the presence of the emitter resistance r_E and the derivation details were illustrated in Appendix A-1. In Eq. 2.0.1, τ_{total} was denoted as the total transit time of the HBT devices while τ_F , the forward transit time, τ_J , the transit time corresponding to the base-emitter (BE) and base-collector (BC) junctions and τ_{RC} , the transit time corresponding to the RC delay contributed by the parasitic resistance and capacitance. In Eq. 2.0.1, the parameters τ_B , τ_E and τ_C were denoted as the base, emitter and collector transit time, respectively. The transit time components which contributed τ_{total} were also illustrated on the respective positions in the schematic cross-section of the HBT device in Figure 2.0.2.



In modern SiGe bipolar technology, both the horizontal and vertical dimensions were scaling down. Under this situation, the dominant factors of the total transit time could be transferred to others. Traditionally, the transit time could be obtained through the relationship between $1/f_T$ and $1/I_C$ illustrated in Figure 2.0.3 schematically. However, the traditional analysis approaches could not decouple the compositions in the total transit time in simple ways. In this section, a simple, robust and efficient approach which could decouple the transit time components were illustrated based on the fundamental devices physics in the following paragraphs.

A. Standard Fabrication Flow and Issues

Figures 2.0.4 illustrated the standard fabrication process an advanced SiGe hetero-junction bipolar transistor, respectively. The buried layer is formed by arsenic ion implantation with dosage $2 \times 10^{15} \text{ cm}^{-2}$ and implantation energy 60 KeV. Next, n-type epitaxy layer deposition with about $2 \times 10^{16} \text{ cm}^{-2}$ phosphorus doping is performed as a selective-implanted-collector (SIC) layer, which improves the high current injection performance. Furthermore, another epitaxy layer doped with germanium and boron is formed to be the base region of the SiGe HBT. The content of germanium and boron atoms in the base region is about 12 % and $4.7 \times 10^{19} \text{ cm}^{-3}$, respectively. The germanium profile shape is designed to be near box-liked and has a plateau concentration near the edge of base collector junction. The peak position of germanium profile is optimized for optimum acceleration efficiency of electron in neutral base region. Finally, heavily arsenic-doped poly-silicon is deposited after the boron-doped epitaxy followed by an activation thermal cycle.

By introducing germanium atoms into the p-type base region, the energy band-gap would be modulated and the effective intrinsic-carrier concentration would increase. If the germanium doping is non-uniform, for example, linear graded doping profile, an excess electric field will be created. The above two phenomena would both contribute the RF characteristics of the devices through improving the DC current

gain β and small signal transit time. The electric field strength is a function of germanium concentration in the p-type base region and its profile. Many studies aimed at the optimization of germanium profile for maximum cutoff frequency [10]-[12]. In addition to germanium profile design, the associated fabrication processes are also the key criterions for realizing high cutoff-frequency device [13]-[15].

Tight process control is desired to prevent the distortion of doping profile suffering from the thermal cycles after the profile definition. One main process, which contributes major profile distortion suffering from thermal budget, is emitter drive-in procedure. In BiCMOS technology, this procedure is also done for source-drain activation. This drive-in and/or activation step involves a large thermal budget. Robust process conditions should be carefully designed for distortion-free doping profile to guarantee high frequency performance.

B. Physics and Theorem

The forward transit time, which consisted of three components: base, emitter and collector transit time, was one of the major indexes for qualifying the RF capability of a bipolar junction transistor. The relationship between the forward transit time and cutoff frequency could be obtained from Eq. 2.0.1 and several device factors

including junction depth, profile shape, peak and edge concentrations of space-charge region, which depend directly and strongly on doping profiles of SiGe HBT, would impact each components of forward transit time. Since some of the device factors above are functions of bias, it is necessary to identify the doping profiles of a SiGe HBT while characterizing its high frequency capability. The concentration of arsenic atoms at the emitter edge is about $2 \times 10^{21} \text{ cm}^{-3}$ with about 20 nm width as the base-emitter junction is forward biased. The peak effective concentration of Boron atoms is about $2 \times 10^{19} \text{ cm}^{-3}$ with about 40 nm intrinsic base width. The near-boxlike germanium profile has a 23 nm-width plateau and the doping concentration on the profile plateau is about 12%, respective to silicon atom concentration. When device dimension scales down to the order of $0.25 \text{ }\mu\text{m}$, the doping profile induced field enhanced acceleration/retarding phenomena would strongly contribute in the quantity of each transit time component [16]. For this reason, doping profile induced field enhancing/retarding effect would be taken into consideration in the transit time analysis.

(I) Field Acceleration and Retarding Effect

The following discussion was based on the reference [16] associated with some modification by the author. Figure 2.0.5 (a) and (b) illustrate the schematic expression

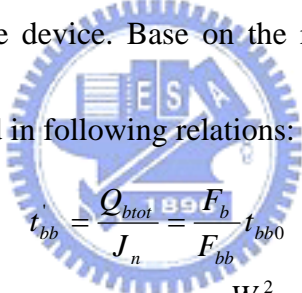
of typical base impurity and the minority carrier distribution for device under normal operation, respectively. The shadow regions between the base and emitter and base and collector doping profiles denote the space charge region of base-emitter and base-collector junctions. The parameters N_1 , N_2 and N_{BC} denote the carrier concentrations at base-emitter junction edge, the peak concentration and the base-collector junction edge, respectively. The horizontal positions $x = 0$, x_{12} and W_b denote the base-emitter junction edge in the base side, the profile peak and the base collector junction edge in the base side, respectively. Thus W_b is also the intrinsic base width. The minority carrier in the intrinsic base region would be divided into two portions Q_{b1} and Q_{b2} according to the horizontal distribution. Q_{b1} denotes the minority carrier within $x = 0$ and x_{12} where the minority carriers transport under a retarding field created by the base doping profile while Q_{b2} denotes the minority carrier within $x = x_{12}$ and W_b where the minority carriers transport under an acceleration field created by the base doping profile. The respective base widths of Q_{b1} and Q_{b2} are W_{b1} and W_{b2} . The charging/discharging velocity for the total base minority carrier Q_{btot} would dominate the base transit time. Associating with the Poisson equations of the junction, the current density J_n and the total base minority carrier Q_{btot} being the sum of Q_{b1} and Q_{b2} and could be estimated from the doping profile [16]:

$$Q_{b1} = qn(0) \frac{W_{b1}}{\ln(r_b)} .$$

$$\begin{aligned}
Q_{b2} &= qn(x_{12})W_{b2} \\
Q_{btot} = Q_{b1} + Q_{b2} &= qn(0)\left[\frac{W_{b1}}{\ln(r_b)} + \frac{W_{b2}}{r_b}\right] \\
J_n &= F_{bb}qn(0)\frac{D_n}{W_b} \\
F_{bb} &= \left(\frac{\eta}{r_b} \frac{W_b}{W_{b2}}\right) \\
r_b &= \frac{N_2}{N_1} = \frac{n(0)}{n(x_{12})} \\
\eta &= \ln\left(\frac{N_2}{N_{bc}}\right)
\end{aligned} \tag{2.0.5}$$

Where F_{bb} denotes the modulation factor of J_n for field acceleration/retarding effects while r_b and η denote the retarding and acceleration factors, which directly related to

the base doping profile of the device. Base on the relations in Eq. 2.0.5, the base transit time could be expressed in following relations:



$$\begin{aligned}
t'_{bb} &= \frac{Q_{btot}}{J_n} = \frac{F_b}{F_{bb}} t_{bb0} \\
t_{bb0} &= \frac{W_b^2}{2D_n} \\
F_b &= \frac{2}{W_b} \left[\frac{W_{b1}}{\ln(r_b)} + \frac{W_{b2}}{r_b}\right]
\end{aligned} \tag{2.0.6}$$

Where D_n denotes the diffusion coefficient of the carrier while the parameter F_b describe the shape of the base doping profile. t'_{bb} denotes the base transit time without considering the effect of germanium doping while t_{bb0} denotes the base transit time of the device with uniform base doping profile. Through the similar approach, the emitter transit time without considering the germanium doping effect could be express in the following relation:

$$\begin{aligned}
t'_{em} &= \frac{Q_{etot}}{J_n} = \frac{F_e}{F_{bb}} t_{em0} \\
t_{em0} &= \frac{W_b W_e}{2D_n} \\
F_e &= \frac{2}{W_e} \left[\frac{W_{e1}}{\ln(r_e)} + \frac{W_{e2}}{2r_e} \right]
\end{aligned} \tag{2.0.7}$$

Where r_e denotes the retarding factor in the emitter region and would be the ration of the effective peak concentration N_{eff} of the emitter profile to the concentration at the emitter-base edge N_0 in the emitter. Like the discussion in the base transit time, F_e describes the profile shape of the emitter profile and plays a weighting role in the emitter transit time estimation. The parameters t_{em0} and t'_{em} denote the transit time of a device with uniform emitter doping and the transit time without the germanium doping effect, respectively. The collector transit time is simply the period for carrier to emitting through the base-collector depletion layer and could be expressed in following relation:

$$t_{scl} \equiv \frac{Q_{c\ tot}}{J_n} = \frac{w_{scl}}{2v_d} \tag{2.0.8}$$

Where the parameter w_{scl} and v_d denote the width of the base-collector space charge depletion layer and the drift velocity of the carrier.

(II) Band-gap Narrowing Effect by Germanium Doping

The following discussion was based on the reference [17] associated with some modification by the author and the box-like germanium doping profile approximation

would be taken into the following discussions. The band-gap narrowing effect impacting the forward transit time would act on the two transit time components: base transit time t_{bb} and emitter transit time t_{em} . The former would be estimated directly by the integral in following formula [17]:

$$\begin{aligned}
 t_{bb0(SiGe)} &\approx \int_0^{W_b} \int_x^{W_b} \exp\left(\frac{R_{gg}}{W_b} x\right) \exp\left(-\frac{R_{gg}}{W_b} x'\right) dx' dx \\
 &= \frac{W_b^2}{2D_n} \frac{2}{R_{gg}} \left\{1 - \frac{1}{R_{gg}} \left[1 - \frac{1}{\exp(R_{gg})}\right]\right\} \\
 &= \frac{1}{F_G} t_{bb0}
 \end{aligned} \tag{2.0.8}$$

And the later is simply contributed by the current density increasing as following:

$$\begin{aligned}
 t_{em(SiGe)} &= \frac{Q_{etot}}{J_n(SiGe)} \approx \frac{Q_{etot}}{\frac{qD_n n_i^2}{N_B} \frac{1}{\int_0^{W_b} \exp\left(-\frac{R_{gg}}{W_b} x\right) dx}} \\
 &= \frac{Q_{etot}}{\frac{qD_n n_i^2}{N_B W_b} \left[\frac{R_{gg}}{1 - \frac{1}{\exp(R_{gg})}} \right]} \\
 &= \frac{Q_{etot}}{J_n F_\beta} \\
 &= \frac{1}{F_\beta} t'_{em}
 \end{aligned} \tag{2.0.9}$$

The parameters presented in Eq. 2.0.8 and 2.0.9 would be illustrated in the following formulas:


$$F_G = \left\{ \frac{2}{R_{gg}} \left\{ 1 - \frac{1}{R_{gg}} \left[1 - \frac{1}{\exp R_{gg}} \right] \right\} \right\}^{-1}$$

$$F_\beta = \frac{R_{gg}}{1 - 1/\exp R_{gg}}$$

$$R_{gg} = \frac{\Delta E_g}{kT} \quad (2.0.10)$$

Where, F_G and F_β describe the modulation effect by germanium profile on emitter transit time and base transit time, respectively and being expressed in term of band-gap narrowing at low current level for device with a box-like base profile. R_{gg} denotes the ratio of ΔE_g over the thermal energy kT and ΔE_g denotes the quantity of band-gap narrowing in the material doped by germanium atoms and which value depends on the content ratio of the germanium atoms. In general, 1 % germanium atoms doping in silicon crystal would bring 7 mV band-gap narrowing.

Finally, the three transit time components would be summery in the following formulas with both field retarding/acceleration effect and band-gap narrowing effect [17]:



$$\begin{aligned}
 t_{bb} &\equiv \frac{Q_{b\ tot}}{J_n} \equiv \frac{1}{F_G} \frac{F_b}{F_{bb}} t_{bb0} \\
 t_{em} &\equiv \frac{Q_{e\ tot}}{J_n} \equiv \frac{1}{F_\beta} \frac{F_e}{F_{bb}} t_{em0} \\
 t_{scl} &= \frac{W_{scl}}{2v_d}
 \end{aligned} \quad (2.0.11)$$

The above relationships give a simple, decoupled and analytical expression for the three transit time components. Each factors presenting in Eq. 2.0.11 could be directly extracted from the SIMS profile.

2.1 Transient Time Distribution

A. Experiment

Based on the relationships from Eq. 2.0.5 to Eq. 2.0.11, we estimated and analyzed forward transit time components according to the practical doping profile. SiGe HBT devices with 0.2 μm emitter width and 10 μm emitter length with various emitter strips were fabricated by 100 GHz SiGe HBT technology. Mathematical tool (Matlab) and device simulator (MEDICI) were used to obtain the solutions from the above complex equations and come out the factors presenting from Eq. 2.0.5 to Eq. 2.0.11. The parameters related to the junctions including W_{b1} , W_{b2} , w_{sc1} , N_0 , N_1 and N_{BC} are extracted from the MEDICI simulation based on the measured SIMS profile. The peak concentration N_{eff} and N_2 in emitter and base region respectively would be directly extracted from the SIMS profile. The drift velocity v_d is set to be 10^7 cm/sec and the band-gap narrowing of the device is about 0.084 eV for 12 % germanium doping. The parameters F_b , F_{bb} , F_e , F_G , F_β , t_{bb0} and t_{em0} are estimated based on the parameters extracted from the doping profile associated with the relations from Eq. 2.0.5 to Eq. 2.0.11 and listed in table 2.1.1. In addition, the practical forward transit time extracted by S parameter measurement methodology coincides with the estimation results. The device was tested under 1 V reverse bias on base-collector junction with different current levels.

B. Analysis

(a) Electric Characteristics of 100 GHz SiGe HBT

Figures 2.1.1 (a) and (b) illustrate the output characteristic and Gummel plot of 100-GHz SiGe-HBT. Figures 2.1.2 and 3 illustrated the high frequency characteristics of 100 GHz SiGe HBT. Figures 2.1.2 (a) and (b) presented the S parameter and bode-plot of SiGe HBT, respectively. Figures 2.1.3 (a) and (b) illustrated the relationship between cutoff frequency f_T and collector current and the relationship between the transit time and collector current, respectively. From Fig. 2.1.3 (a), the current level, at which Kirk effect occurs, is about 10 Amperes. From Fig. 2.1.3 (b), the intersection of $1/f_T$ in $0.2 \times 10^{-2} \mu\text{m}^2$ was about 1.42 picosecond. The practical electric characteristics would be taken as the benchmark of following estimation accuracy.

(b) Transit Time Analysis

The relationship between practical measurements of forward transit time of SiGe HBT with 100 GHz cutoff frequency versus collector current is illustrated in Fig. 2.1.3 (b). The approximated forward transit time value for qualitatively characterizing the compositions was illustrated in Table 2.1.1 according to the relationships from 2.0.5 to 2.0.11. In Fig. 2.1.3 (b), the linear intersection of $1/f_T$ value from low current

region of device in $02 \times 10 \times 2 \mu\text{m}^2$ was approximately 1.42 ps, which should be the sum of the forward transit time τ_F and the RC delay time τ_{RC} . As a result, the forward transit time τ_F obtained by the estimation approach was about 1.06 ps. The values of estimated τ_F and simulated τ_{RC} could be qualitatively verified from the data illustrated in Fig. 2.1.3 (b) and the formula illustrated as follow:

$$\begin{aligned}
 \text{For } 02 \times 10 \times 1 \mu\text{m}^2 \quad \text{Device} \quad \tau_{\text{intersection}} &= \tau_F + \tau_{RC1} \\
 \text{For } 02 \times 10 \times 2 \mu\text{m}^2 \quad \text{Device} \quad \tau_{\text{intersection}} &= \tau_F + \tau_{RC2} \\
 \text{For } 02 \times 10 \times 4 \mu\text{m}^2 \quad \text{Device} \quad \tau_{\text{intersection}} &= \tau_F + \tau_{RC4} \quad (2.1.1)
 \end{aligned}$$

Where τ_{RC1} , τ_{RC2} , τ_{RC4} illustrated the RC delay components. The order of the estimated τ_F of 1.06 ps was fairly acceptable as the basis for further discussing the weighting of τ_B , τ_E and τ_C in τ_F in the following paragraph.

From the analysis above the weighting of the base transit time is still dominant compared to the other two, the collector transit time grown up compared to those in early generation [16] and the shrinkage of boron profile associated with the reducing boron concentration may be responsible for this result. Second, the collector transit time could be comparable in quantity to the emitter transit time. With decreasing emitter width and the benefit from germanium doping, the emitter transit time dramatically drops. As a result, the development of high frequency capability of a SiGe HBT in next generations, the emitter profile and collector profile would be

important issues. More heavily doped and narrower width profile would be the candidates for emitter and collector region.

The transit time of 100 GHz SiGe HBT was analyzed with practical SIMS profile to obtain each quantity weighting of three major components of forward transit time: the base transit time, emitter transit time and collector transit time. The numerical estimation result was conformed using S parameter measurement and showed qualitatively coincidence. The analysis result shows that the weightings of collector transit time has grown up compared to the earlier generations. This component would play more important roles in developing future high frequency SiGe HBT. Tight profile control would be a very important issue for high frequency device development.

2.2 Geometry Dependency of Cutoff Frequency

Based on the discussion above, the ration of collector transit time in total device transit time could be even grow in future technologies in which the base doping profile would be continuously narrower and concentrated. As a result, the role of the collector could be further important in the electrical characteristics of the SiGe HBT devices in several ways including the fundamental RF property, cutoff frequency f_T

(and transit time as well), maximum oscillation frequency f_{\max} , RF noise figure and linearity. In this section, the geometry dependency of the cutoff frequency f_T was firstly discussed for 120 GHz SiGe bipolar technology.

In Figure 2.2.1 the relationship between cutoff frequency f_T and current density J_C for HBT devices in various emitter widths were illustrated. Theoretically, the forward transit times for devices in various dimensions fabricated by the fixed technology should be consistent. Such theoretical basis could not explain the measurement results illustrated in Fig. 2.2.1 in which, the peak cutoff frequency was larger for devices with smaller emitter width since the base pushing out effect took place at larger collector current density.



The physical origins of the phenomenon discovered in Fig. 2.2.1 could be qualitatively obtained from Figures. 2.2.2 (a) and (b) in which the current flux distribution in the collector region of HBT devices in various emitter widths (W_E) under fixed J_C values were illustrated. In Fig. 2.2.2 (a), the narrower emitter one, the current could spread out toward the collector contacts. Such current spreading decreased the current density (J_C') in the collector region compared with J_C value. Similar current spreading could take place in the wider HBT device illustrated in the right hand side of Fig. 2.2.2 (a). However, for the wider device (Fig. 2.2.2 (b)), the current density decrease in the collector region could be less significant since the

relative larger emitter area. For this reason, comparing to the wider emitter devices, larger J_C should be needed for inverting the electrical polarity of the device for narrow emitter device. In other words, the base pushing-out effect (Kirk effect) could take place at higher J_C for devices with smaller emitter width.

The geometry dependent property of the f_T - J_C characteristic could impact the operating stability and product performance of radio frequency circuit if the device RF model failed to include the collector spreading current effect into the device model. In the above section, we developed a simple and physical mechanism to model the behavior that was observed in Fig. 2.2.1. This research could be valuable for device and circuit designer to develop even stable and high quality products.



2.3 Device Characteristics on Epitaxy thickness Effect

For higher power capability in RF applications the breakdown performance of SiGe HBT devices were usually improved by increasing the epitaxy thickness of the n^- region, which constructed the collector region of the devices. However, it could tradeoff the cutoff frequency value of the device. In addition to the above impact, the increase of n^- epitaxy thickness could also result in the delay of the Kirk effect. Figures 2.3.1 (a) and (b) illustrated the relationship between f_T and J_C of H and L group devices, respectively. In Figs. 2.3.1, the collector current density level J_K at

which the Kirk effect took place was higher for the device with thicker collector epitaxy layer. The physics could be deduced associated with Figures 2.3.2 (a) and (b) in which the current flux in the collector region for devices with various collector thicknesses were illustrated. For the same operation collector current density J_C , the current spreading in the collector region could be more significant for devices with thicker epitaxy layer. For this reason, the corresponding J_C' could be relatively lower. As a result, the current density J_K was higher than that of the device with thinner epitaxy layer as illustrated in Fig. 2.3.1.

The behavior of Kirk effect delay described above could be also modulated by the collector concentration levels. In Figures 2.3.3, the f_T - J_C relationships of devices with higher selective collector implant (SIC) concentration levels were illustrated. The corresponding current flux spreading in the collector region of the higher collector doping levels (L and H group) were illustrated in Figure. 2.3.4 (a) and (b) respectively. Comparing the information from Figs. 2.3.1 (a) to 2.3.4 (b), the Kirk effect delay phenomenon behaved less significantly for devices with higher SIC concentration against the Epitaxy thickness variation. It could be extremely possible that the current spreading effect in the collector region have been suppressed by the high concentration SIC layer since the high-concentration collector provided a even lower resistive current path so as to “tighten” the carrier flux.

Similarly, in this section, we also provided the collector doping dependency of the current flux spreading in the collector region. It could be a valuable topic for the following researcher that would include such effect into a SPICE comparable model.

2.4 Conclusion

In this chapter, the composition of the transit time τ_{total} and the forward transit time τ_F of 100 GHz has been discussed. The study results could help the device designer to even understand the details of the transit time components so as to design an optimum doping profile of the HBT device in the next generations. Besides, the bias dependency of the cutoff frequency f_{T-J_C} was also illustrated in this section. It was identified that, the device dimension, collector epitaxy thickness and collector doping level could alter the degree of current spreading in the collector region so as to modulate the current density level at which the Kirk effect took place. Such physical behavior could be included in the SPICE comparable model, which could reflect the Kirk effect delay effect. It could be very valuable for circuit designer to design the bias network properly to ensure the transistor was operated under an accurate condition.

Appendix A.2

Based on the fundamental circuit theorem, the current gain h_{FE}' could be obtained

in terms of the components illustrated in Figure 2.0.1:

$$h_{jE}' = \frac{i_C'}{i_B} = \frac{C - B}{A'C + A + B + 1} \quad (\text{A.2.1})$$

Where

$$A' = \frac{Z_o'}{Z_\mu} \quad (\text{A.2.2})$$

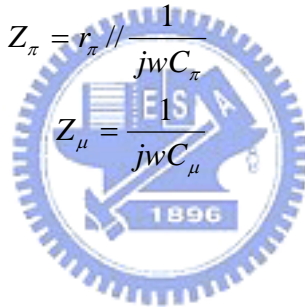
$$B = \frac{Z_\pi}{Z_\mu} + (1 + g_m Z_\pi) \frac{r_E}{Z_\mu} \quad (\text{A.2.3})$$

$$C = g_m Z_\pi \quad (\text{A.2.4})$$

$$Z_o' = (r_C + R_L) \quad (\text{A.2.5})$$

$$Z_\pi = r_\pi // \frac{1}{j\omega C_\pi} \quad (\text{A.2.6})$$

$$Z_\mu = \frac{1}{j\omega C_\mu} \quad (\text{A.2.7})$$



Thus

$$h_{jE} = \frac{g_m Z_\pi - \left[\frac{Z_\pi}{Z_\mu} + (1 + g_m Z_\pi) \frac{r_E}{Z_\mu} \right]}{g_m Z_\pi \frac{Z_\pi}{Z_\mu} + \frac{Z_C}{Z_\mu} + \frac{Z_\pi}{Z_\mu} + j\omega C_\mu Z_\pi [1 + g_m (Z_\pi + r_E)]} \quad (\text{A.2.8})$$

Where

$$Z_\mu = \frac{1}{j\omega C_\mu} \quad (\text{A.2.9})$$

$$Z_\pi = \frac{r_\pi}{1 + j\omega r_\pi C_\pi} \quad (\text{A.2.10})$$

$$Z_C = r_C \quad (\text{A.2.11})$$

Then

$$h_{fE} = \frac{[g_m - j\omega C_\mu(1 + g_m Z_\pi)]r_\pi - j\omega C_\mu r_E(1 + j\omega C_\pi r_\pi)}{[1 + j\omega C_\mu(Z_C + r_E)](1 + j\omega C_\pi r_\pi) + j\omega C_\mu r_\pi[1 + g_m(Z_\pi + r_E)]} \quad (\text{A.2.12})$$

$$h_{fE} \approx \frac{g_m r_\pi + j\omega\{-[r_E + (1 + g_m r_E)r_\pi]C_\mu\}}{1 + j\omega\{r_\pi C_\pi + [1 + g_m(r_E + r_C)]r_\pi C_\mu\}} \quad (\text{A.2.13})$$

$$h_{fE} \approx \frac{g_m r_\pi}{j\omega\{r_\pi C_\pi + [1 + g_m(r_E + r_C)]r_\pi C_\mu\}} \quad (\text{A.2.14})$$

$$h_{fE} \approx \frac{g_m}{j\omega\{C_\pi + [1 + g_m(r_E + r_C)]C_\mu\}} \quad (\text{A.2.15})$$

Based on the definition of the cutoff frequency:

$$\omega_T \approx \frac{g_m}{C_\pi + [1 + g_m(r_E + r_C)]C_\mu} \quad (\text{A.2.16})$$

Then

$$\frac{1}{\omega_T} \approx \frac{1}{g_m} \{C_\pi + [1 + g_m(r_E + r_C)]C_\mu\} \quad (\text{A.2.17})$$

Where

$$C_\pi = C_{DE} + C_{BE} \quad \text{and} \quad C_\mu = C_{BC} \quad (\text{A.2.18})$$

Thus

$$\tau_{total} = \frac{1}{\omega_T} = \frac{1}{g_m} \{C_{DE} + C_{BE} + C_{BC} + g_m(r_E + r_C)C_{BC}\} \quad (\text{A.2.19})$$

$$\tau_{total} = \frac{1}{\omega_T} = \tau_F + \tau_J + \tau_{RC} \quad (\text{A.2.20})$$

Where

$$\tau_F = \frac{C_{DE}}{g_m} \quad (\text{A.2.21})$$

$$\tau_J = \frac{V_T}{I_C}(C_{BE} + C_{BC}) \quad (\text{A.2.22})$$

$$\tau_{RC} = (r_C + r_E)C_{BC} \quad (\text{A.2.23})$$

References

- [1] H. Schumacher and U. Erben, "Heterojunction bipolar transistors for noise-critical applications", in *proceedings of XVIII SOTAPOCS*, vol. 93-27, 1993, pp. 345-352.
- [2] A. Schüppen, H. Dietrich, S. Gerlach, H. Köhnemann, J. Arndt, U. Seiler, R. Götzfried, U. Erben, and H. Schumacher, "SiGe-technology and components for mobile communication systems", in *Proceedings of 1996 Bipolar BiCMOS Circuit and Technology Meeting*, 1996, pp. 130-134.
- [3] M. Soyuer, J. O. Plouchart, H. Ainspan and J. Burghartz, "A 5.8-GHz 1-V Low-Noise Amplifier in SiGe Bipolar Technology", *Proc. 1997 IEEE RFIC Symp.*, pp. 19-22, June, 1997.
- [4] P. J. Wijnen and R. D. Gardner, "A new approach to optimizing the base profile for high-speed bipolar transistors", *IEEE Electron Device Lett.*, vol. 11, pp. 149-152. 1990.
- [5] J. Song and J. S. Yuan, "Comments on "On the profile design and optimization of epitaxial Si and SiGe-base bipolar transistor technology for 77 K applications—Part I: Transistor DC design considerations," *IEEE Trans. Electron Devices*, vol. 40, pp. 525-541, 1993.
- [6] G. L. Patton, J. H. Comfort, B. S. Meyerson, E. F. Crabbe, G. L. J. Scilla, E. de

Fresart, J. M. C. Stork, J. Y. C. Sun, D. L. Hareme, and J. Burghartz, "63-75 GHz f_T SiGe-base heterojunction bipolar technology", in *1990 Sump. VLSI Technology Tech. Dig.*, pp. 49-50.

[7] D.M. Rechev, J. D. Cressler, and A. J. Joseph, "Scaling issues and Ge profile optimization in advanced UHV/CVD SiGe HBT's," *IEEE Trnas. Electron Devices*, vol. 44 pp. 431-440, Mar. 1997.

[8] T. Chen, C. T. Chuang, G. P. Li, S. Basavaiah, D. D. Tang, M. B. Ketchen, and T. H. Ning, "An advanced bipolar transistor with self-aligned ion-implanted base and w/poly emitter", *IEEE Trans. Electron Devices*, vol. 35, pp. 1322-1327, 1988.

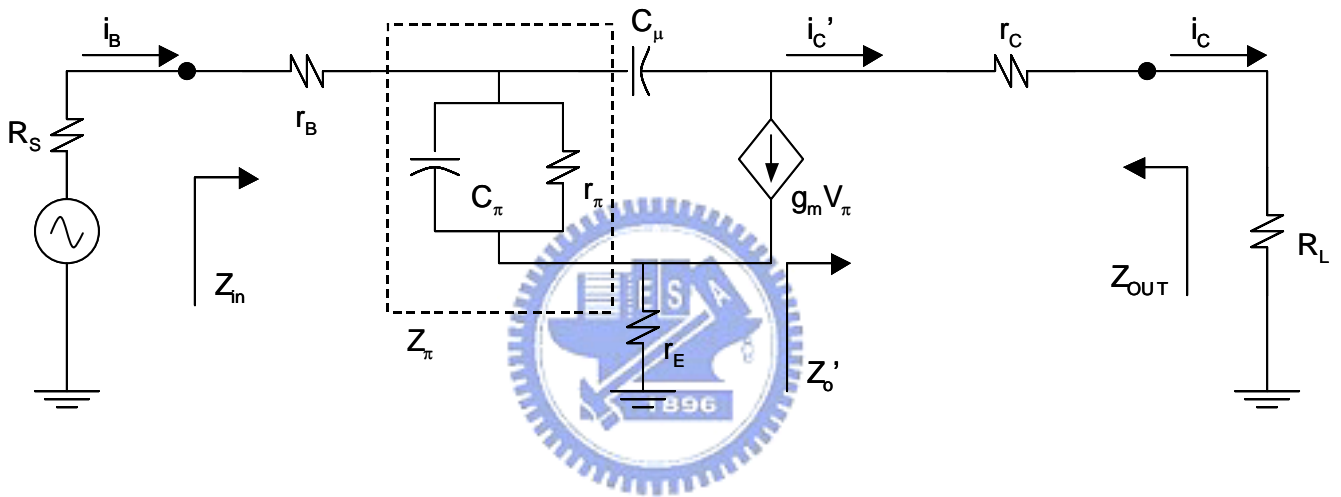
[9] T. Yamaguchi, Y. S. Yu, E. E. Lane, J. S. Lee, E. E. Patton, R. D. Herman, D. R. Ahrendt, V. F. Drobny, T. H. Yuzuriha, and V. E. Gruts, "Process and device performance of a high-speed double poly-Si bipolar technology using boron-poly process with coupling-base implant", *IEEE Trans. Electron Devices*, vol. 35, pp. 1247-1256, 1988.

[10] P. F. Lu, J. H. Comfort, D. D. Tang, B. S. Meyerson, and J. Y. C. Sun, "The implementation of a reduced-field profile design for high-performance bipolar transistors", *IEEE Electron Device Lett.*, vol. 11, pp. 336-338, 1990.

[11] Kamins, T. I., "Pattern sensitivity of selective $\text{Si}_{1-x}\text{Ge}_x$ chemical vapor deposition: Pressure dependence", *J. Appl. Phys.*, vol. 74, no. 9, pp. 5799, Nov. 1993.

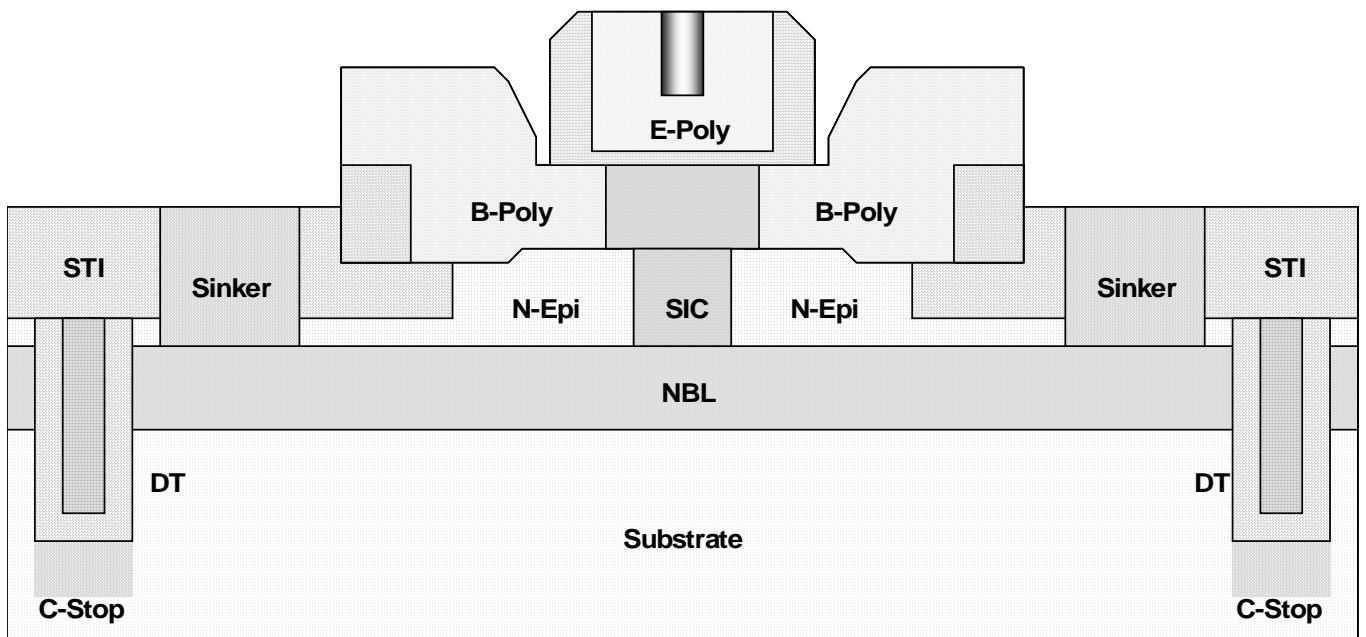
- [12] Prinz, E. J. Sturm, "Current Gain-Early Voltage Products in Heterojunction Bipolar Transistors with Nonuniform Base Bandgaps", *J. IEEE Electron Device Lett.*, EDL-12, 42. Vol. 12, no. 12, Dec.1991.
- [13] Ryum, B. R., and Han, T.-H., "MBE-grown SiGe base HBT with polysilicon-emitter and TiSi₂ base ohmic layer", *Solid State Electron.*, vol. 39, no. 11, pp. 1643, Nov. 1996.
- [14] G. L. Patton, S. S. Iyer, S. L. Delage, S. Tiwari, and J. M. C. Stork, "Silicon-germanium-base heterojunction bipolar transistors by molecular beam epitaxy", *IEEE Electron Device Lett.*, vol. 9, pp. 165-167, Apr. 1988.
- [15] G. L. Patton et al., "SiGe-base, poly-emitter heterojunction bipolar transistors", in *Symp. VLSI Technol. Dig. Tech. Papers*, May 1989, pp. 95-96.
- [16] David J. Roulston, "Bipolar Semiconductor Device," pp.220-224, 1990.
- [17] Yuan Taur, "Fundamentals of Modern VLSI Devices", pp. 360-380, 1998

Figures and Tables of Chapter 2



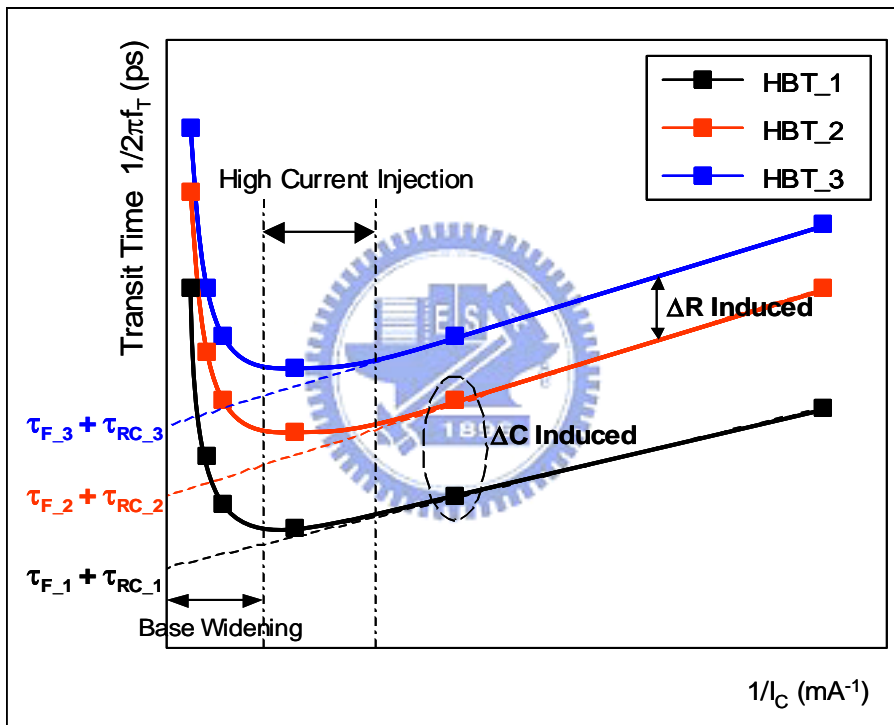
Small signal model of bipolar transistor with emitter resistance

Figure 2.0.1



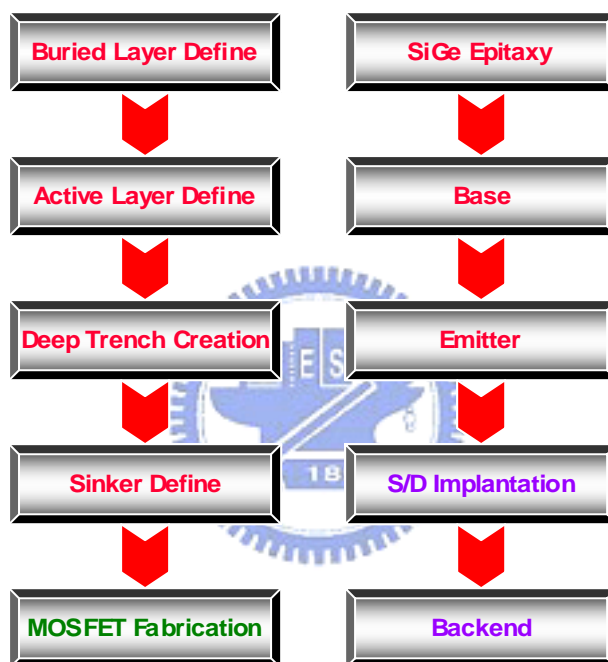
Cross-section of view of SiGe HBT with single emitter fabricated by 0.18 μm BiCMOS technology

Figure 2.0.2



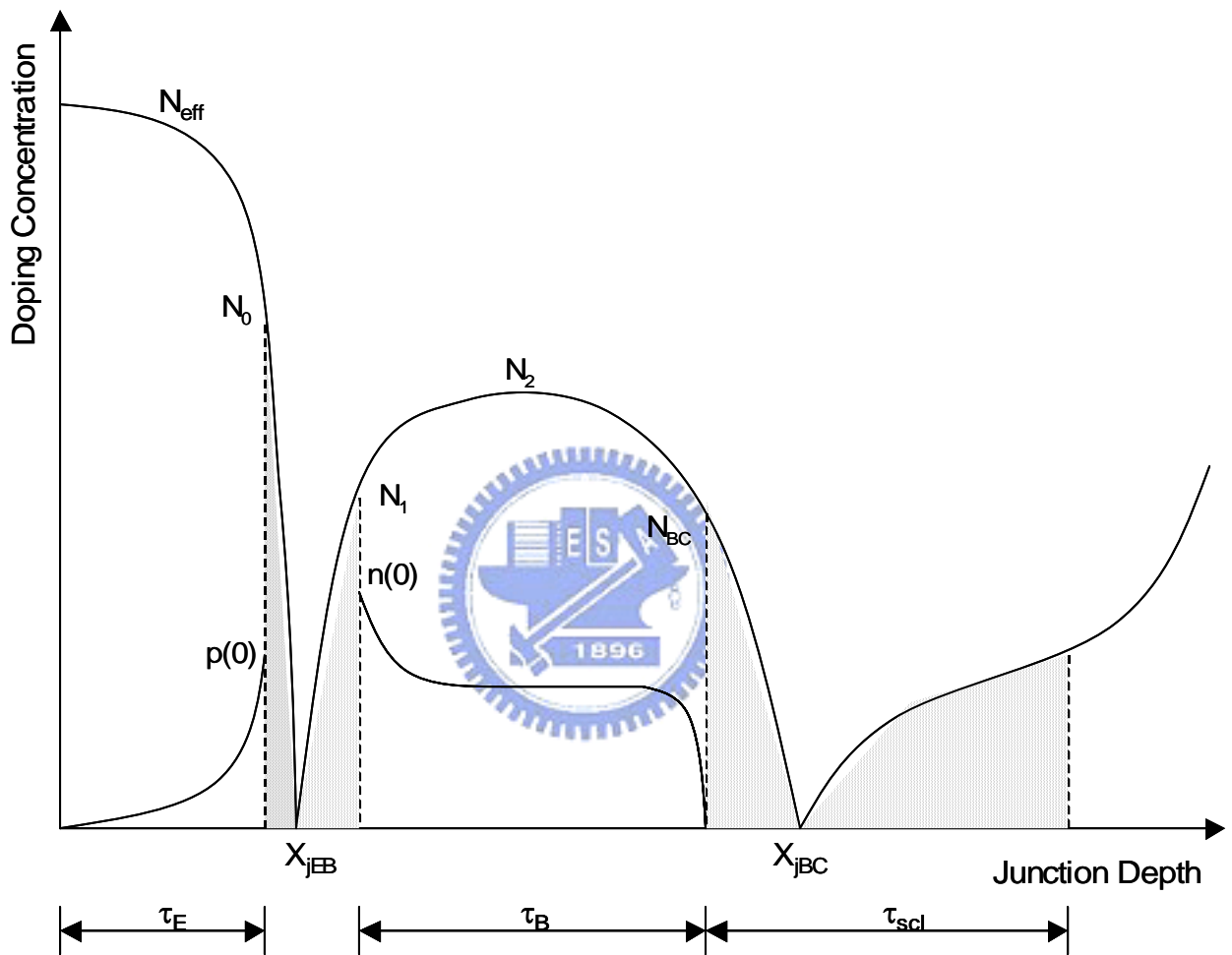
Traditional approach to extract the forward transit time of a bipolar device.

Figure 2.0.3



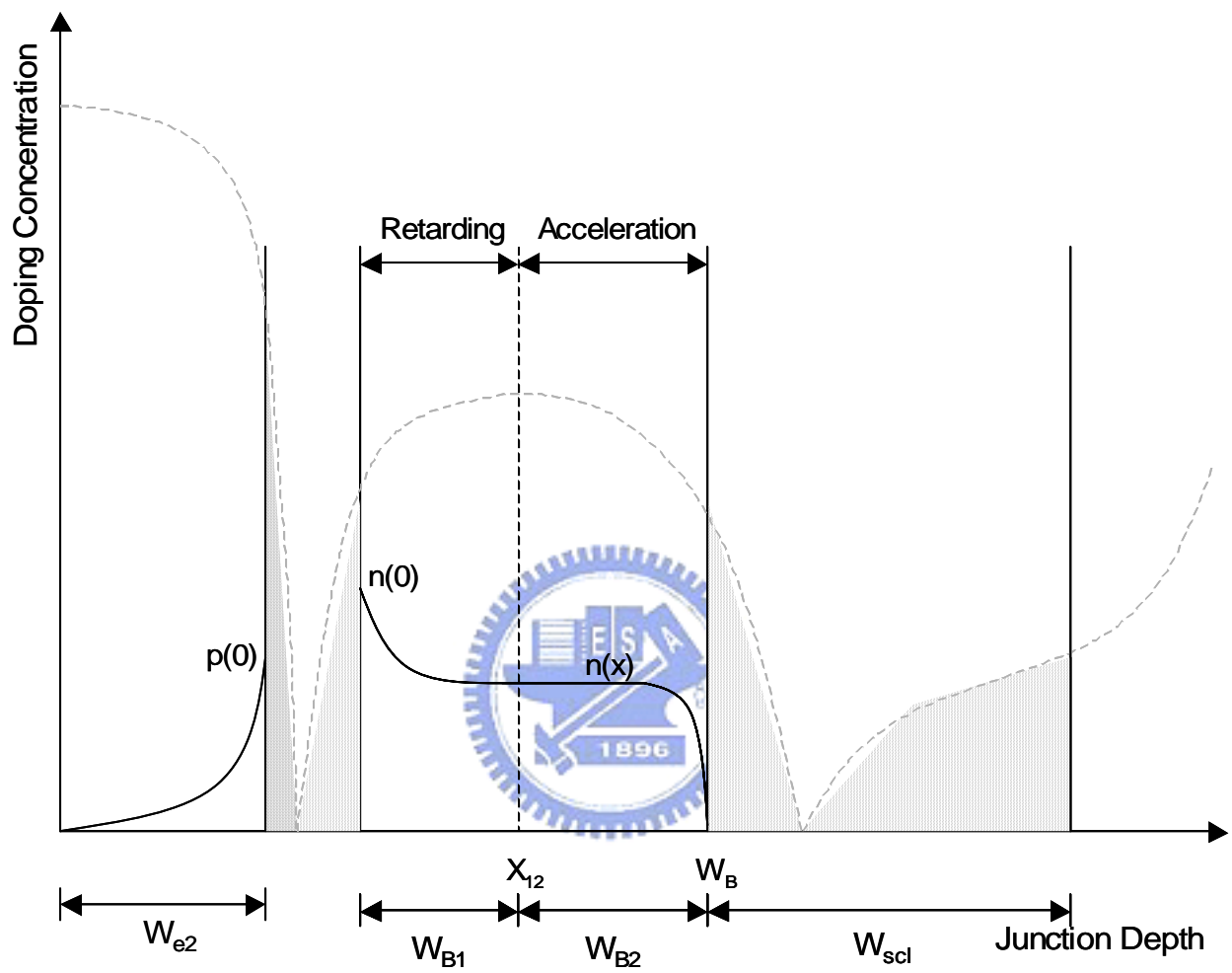
Fabrication process of standard BiCMOS fabrication process

Figure 2.0.4



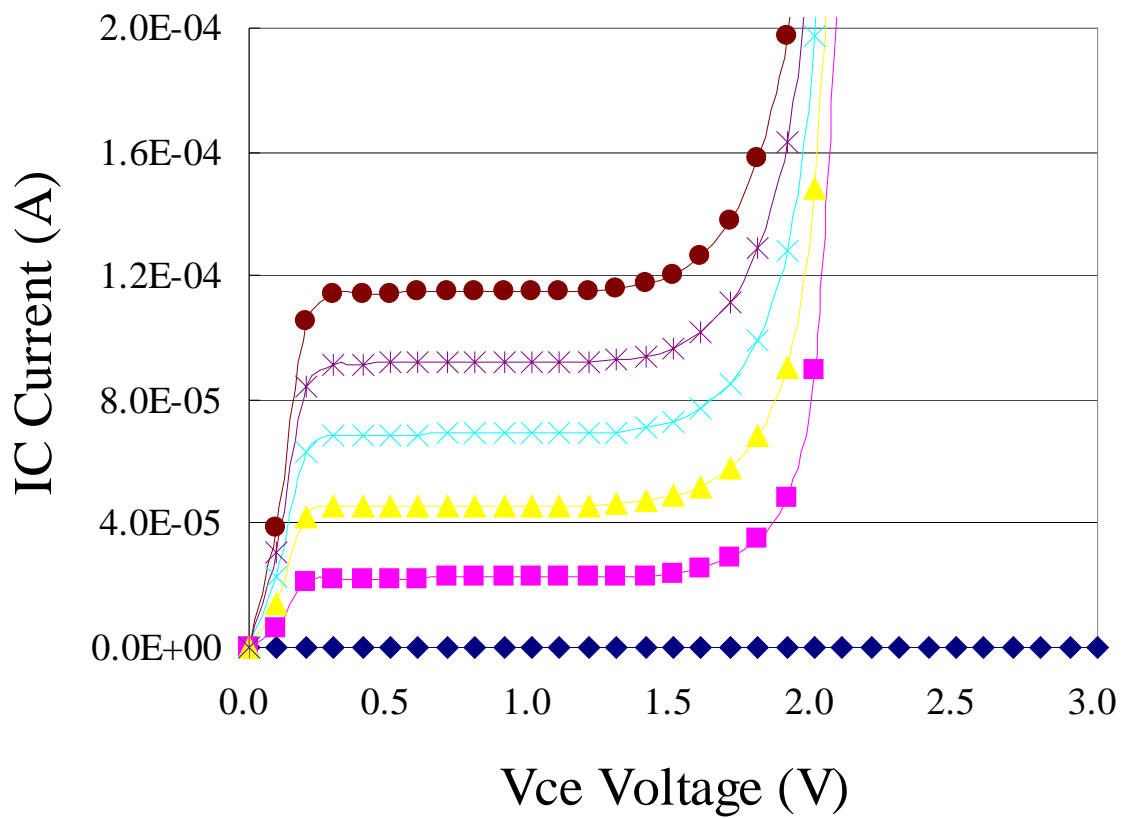
Key parameters of doping profile for transit time estimation

Figure 2.0.5 (a)



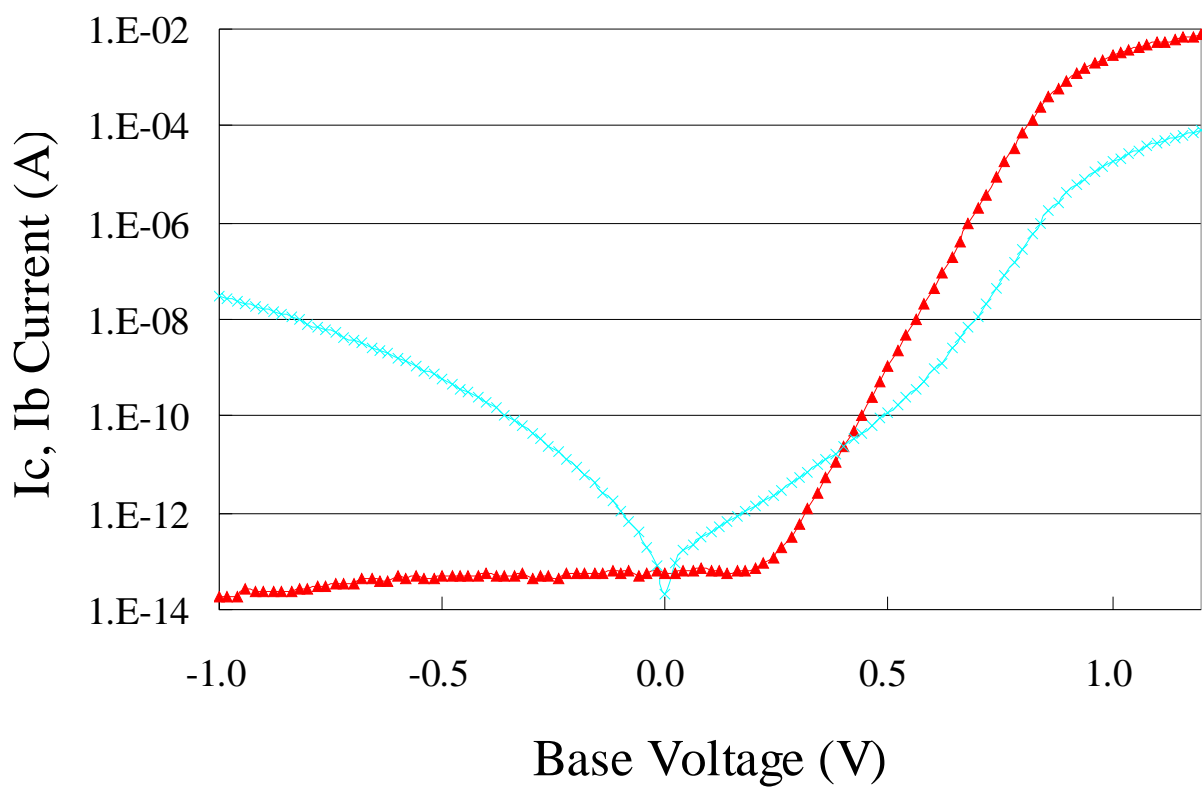
Minority carrier distribution of bipolar device and the field effect induced by the majority carrier in the base region

Figure 2.0.5 (b)



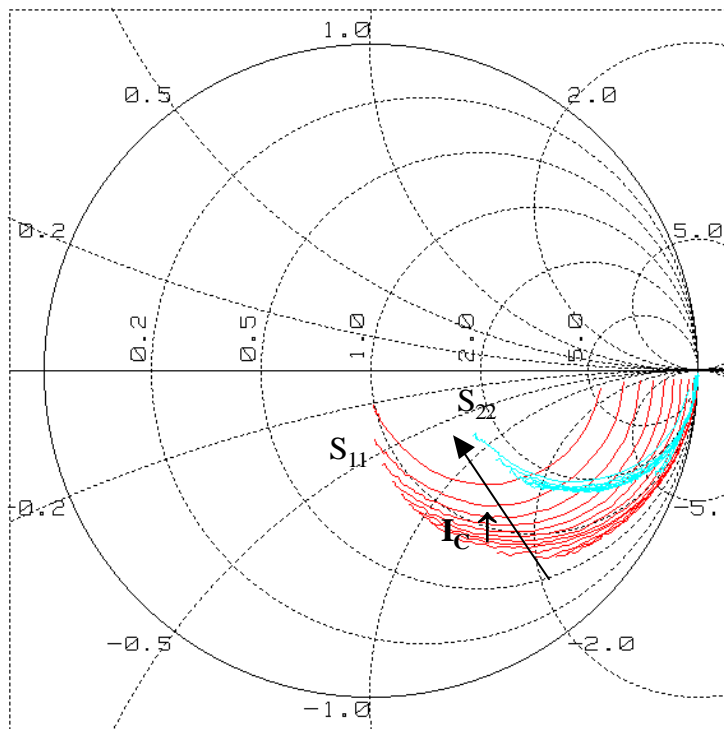
Output characteristics of H-group SiGe HBT in $0.2 \times 10 \times 1 \mu\text{m}^2$

Figure 2.1.1 (a)



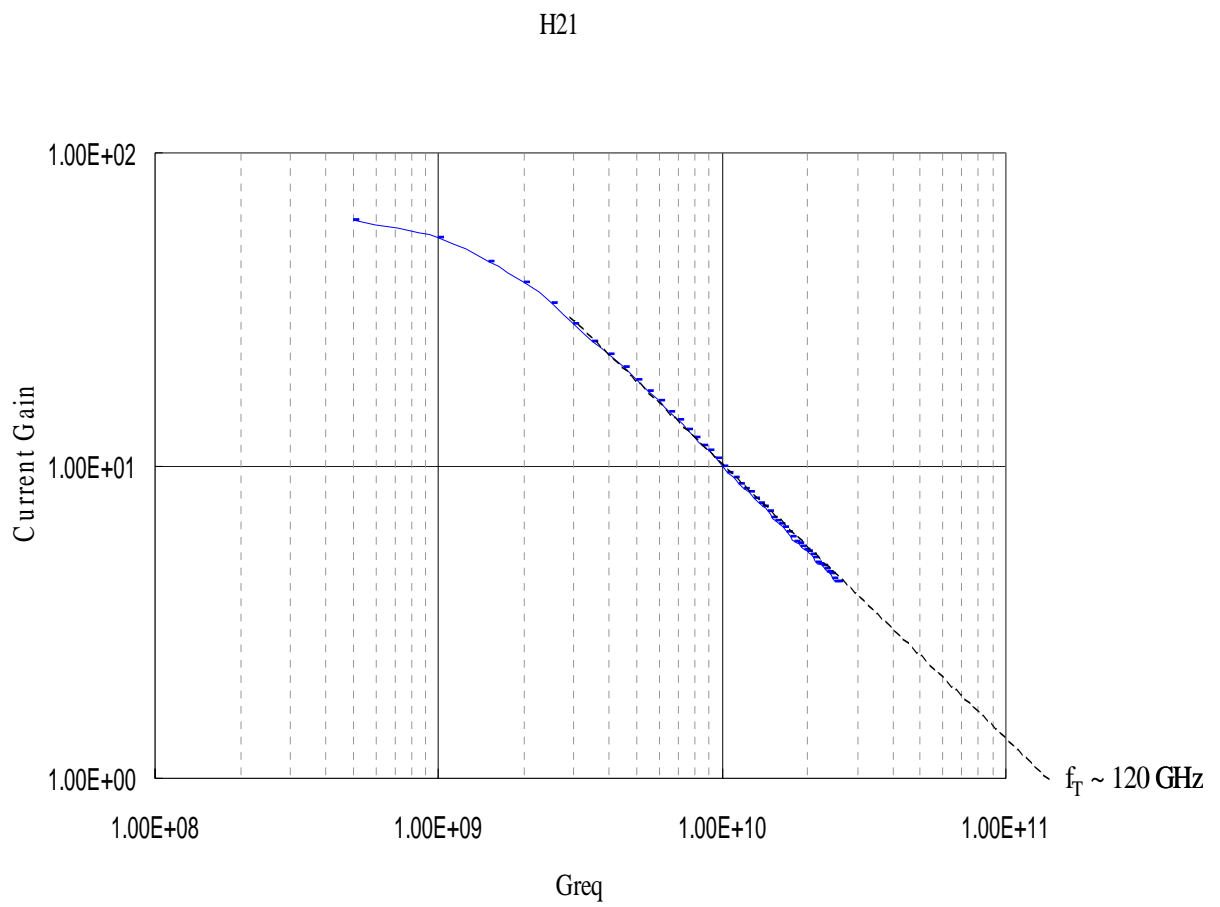
Gummel plot of H-group SiGe HBT in $0.2 \times 10 \times 1 \mu\text{m}^2$

Figure 2.1.1 (b)



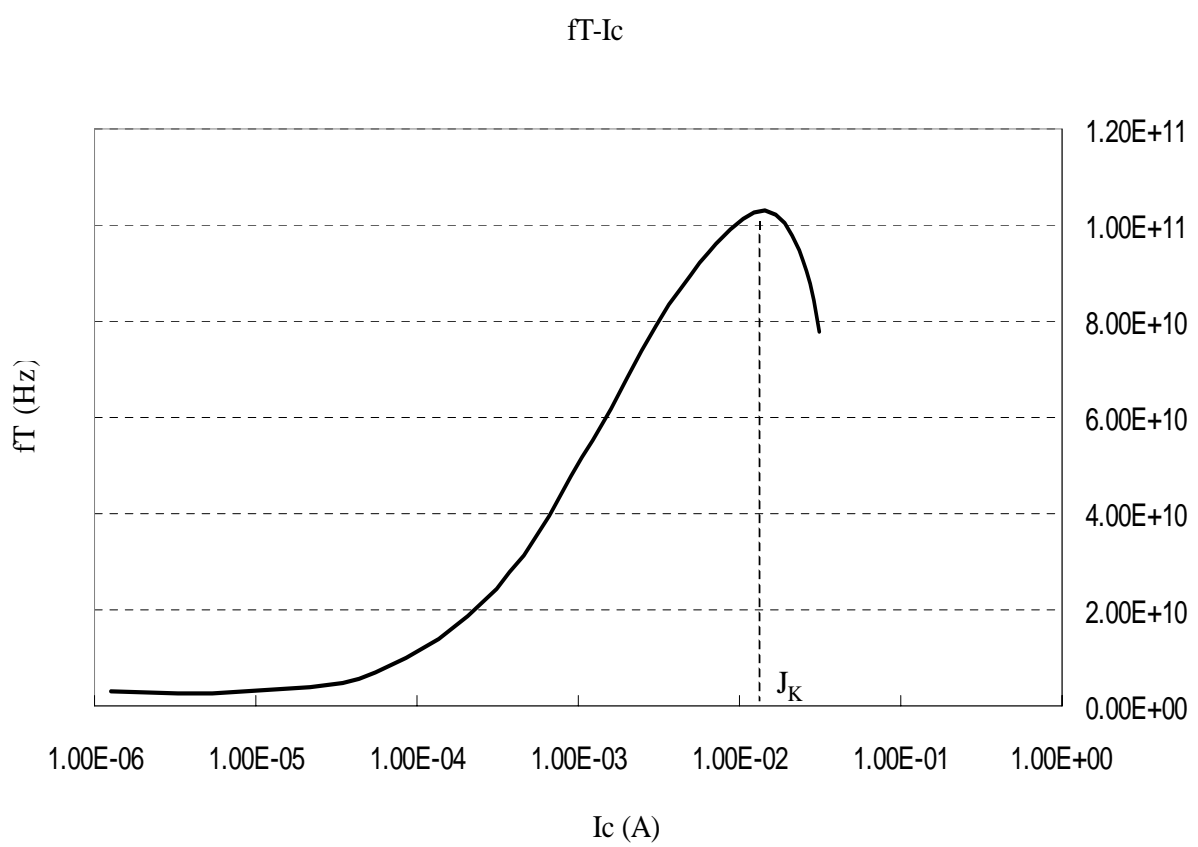
Bias dependent input and output scattering parameters of H-group SiGe HBT in $0.2 \times 10 \times 1 \mu\text{m}^2$

Figure 2.1.2 (a)



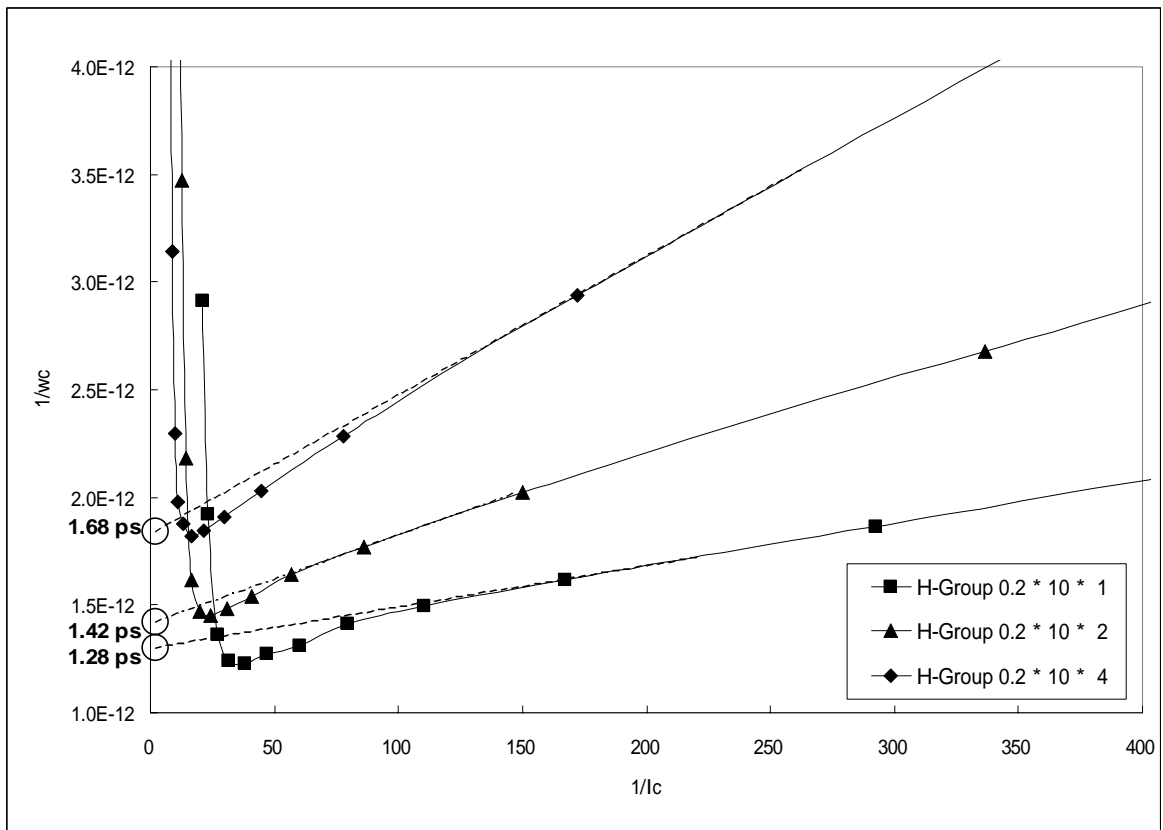
Short circuit current gain and corresponding cutoff frequency of H-group SiGe HBT
in $0.2 \times 10 \times 1 \mu\text{m}^2$ under V_{BE} 0.9 volt and V_{BC} 1 volt

Figure 2.1.2 (b)



Cutoff frequency versus collector current of H-group SiGe HBT in $0.2 \times 10 \times 1 \mu\text{m}^2$ with V_{BC} 1volt

Figure 2.1.3 (a)



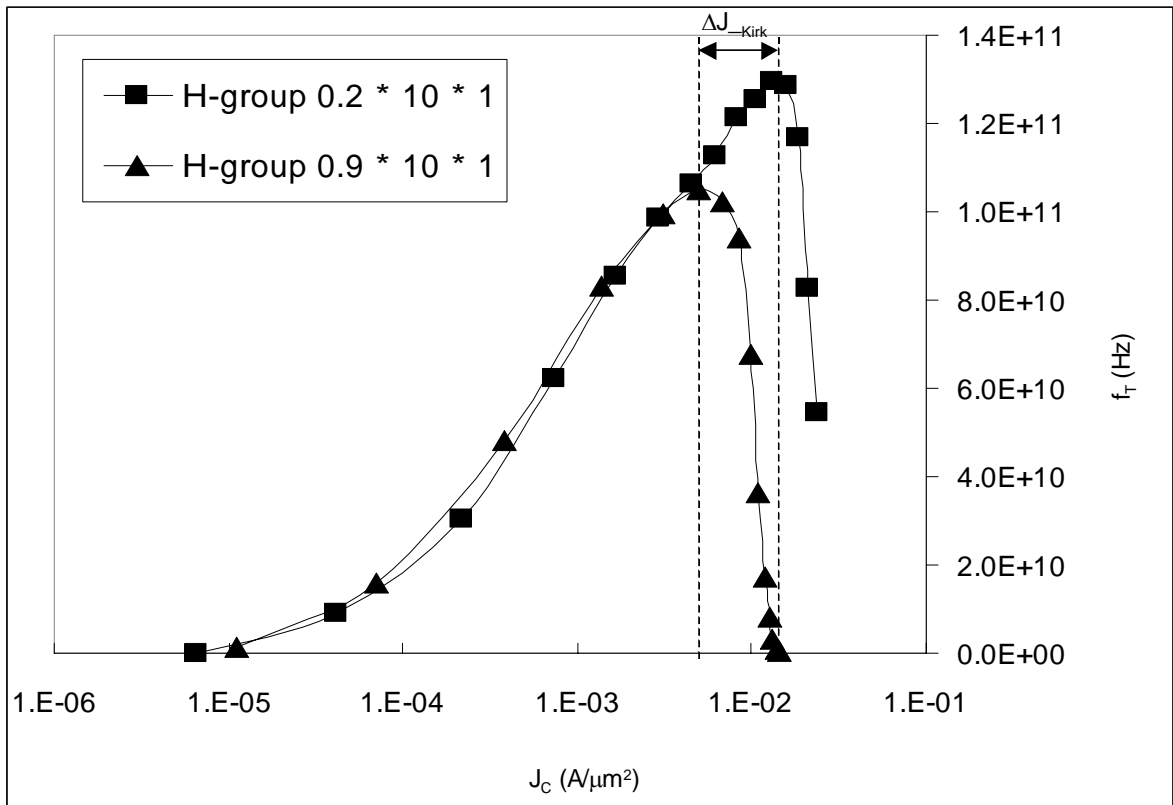
$1/f_T$ - $1/I_C$ relationships of HBT devices with $0.2 \times 10 \times 1, 2$ and $4 \mu\text{m}^2$

Figure 2.1.3 (b)

Base				
Wb1	Wb2	N1	N2	Nbc
2.4E-06	2.E-06	9.E+18	2.E+19	5.E+17
Wb	rb (Ret Coef)		Ita (Acceleration Coef)	
4.40E-06	2.22E+00		3.69E+00	
Fb	Fbb	Fg	Rgg	
1.78	3.65	2.36	3.36	
tbb0	tbb'	tbb(SiGe)		
3.53E-12	1.71E-12	7.27E-13		
Emitter				Collector
We1	We2	Neff	N0	Wsc1
2.00E-06	2.E-06	1.E+20	1.2E+19	7.2E-06
We		re (Ret Coef)		tsc1
3.60E-06		8.33E+00		2.63E-13
Fe		Fbeta	Rgg	
0.29		3.48	3.36	Total
tem0	tem'	tem(SiGe)		ttot
2.88E-12	2.28E-13	6.55E-14		1.06E-12

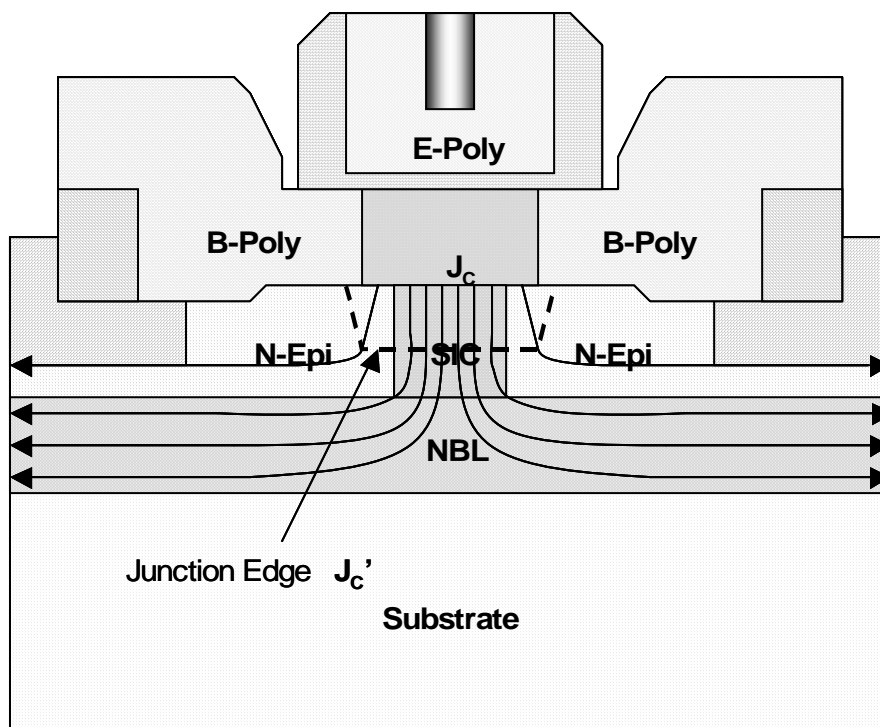
Estimation results of the components of forward transit time and the corresponding physical factors presented in the method

Table 2.1.1



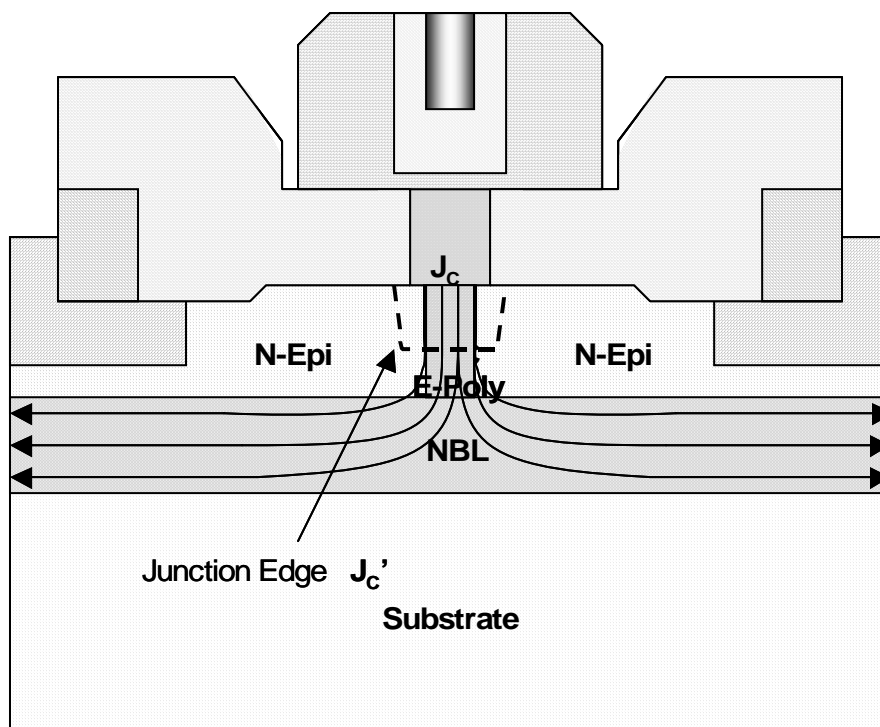
f_T - J_C relationships of H-group SiGe HBT devices in $0.2 \times 10 \times 1$ and $0.9 \times 10 \times 1 \mu m^2$

Figure 2.2.1



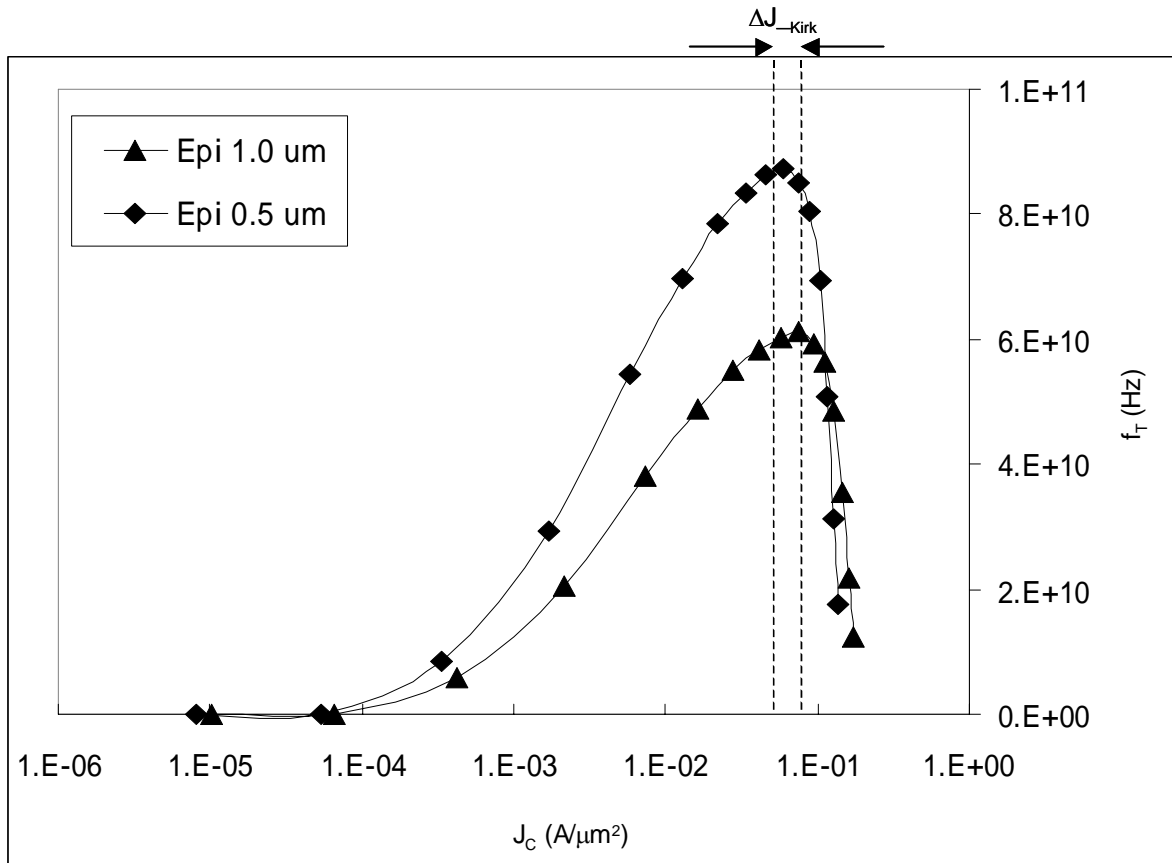
Current spreading in the collector region of device with larger emitter width

Figure 2.2.2 (a)



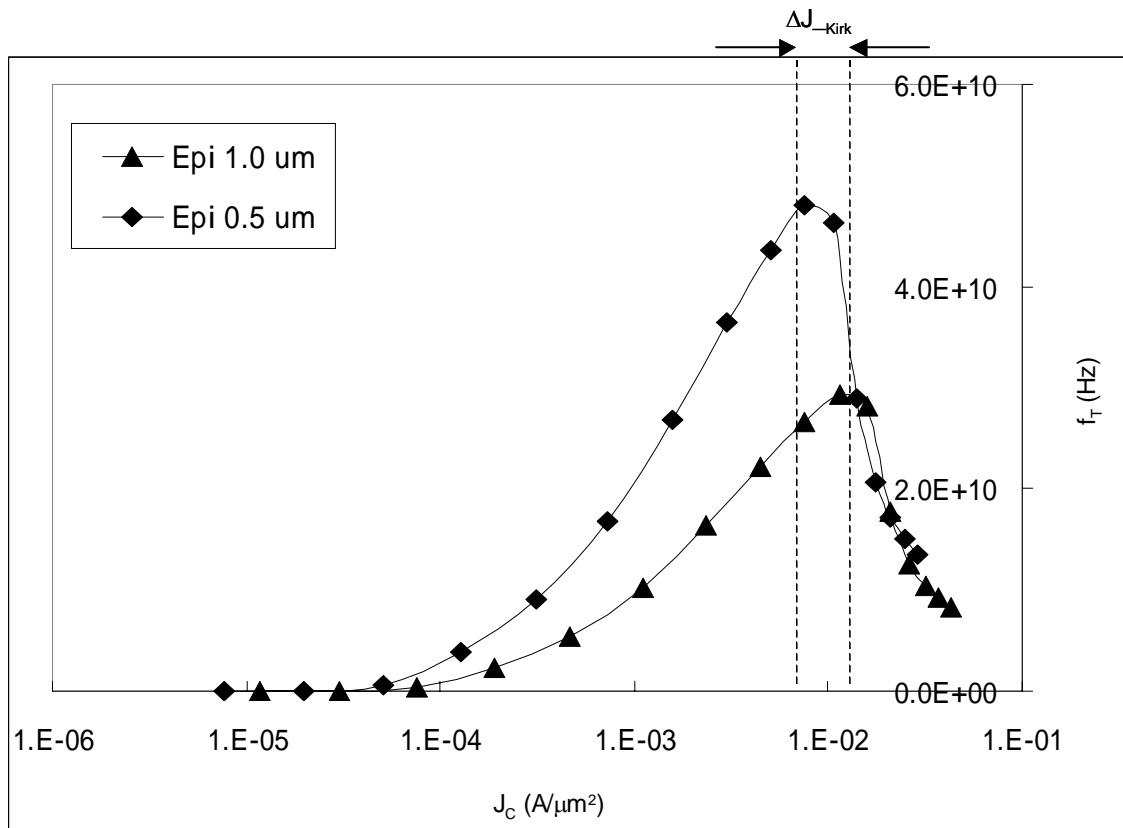
Current spreading in the collector region of device with smaller emitter width

Figure 2.2.2 (b)



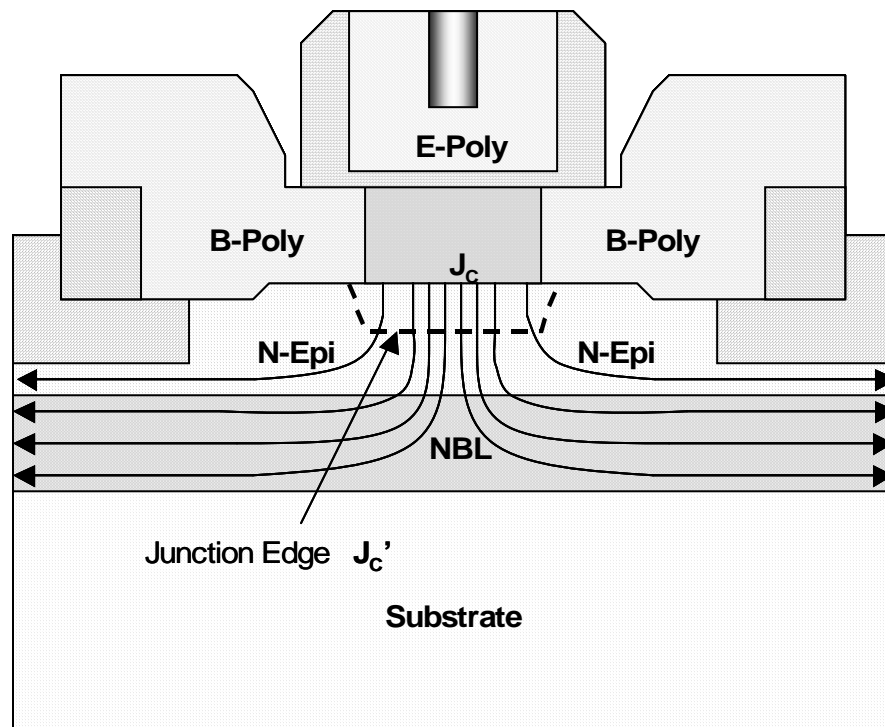
f_T - J_C relationships of H-group SiGe HBT devices in $0.2 \times 10 \times 4 \mu m^2$ with various collector epitaxy thickness 0.5 and 1 μm

Figure 2.3.1 (a)



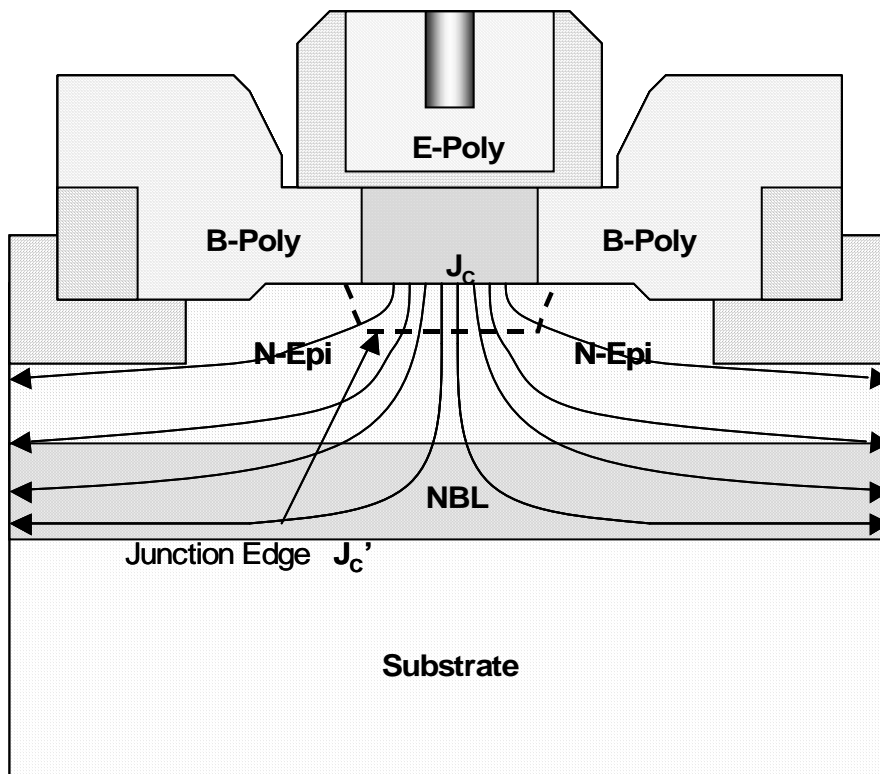
f_T - J_C relationships of L-group SiGe HBT devices in $0.2 \times 10 \times 4 \mu m^2$ with various collector epitaxy thickness 0.5 and 1 μm

Figure 2.3.1 (b)



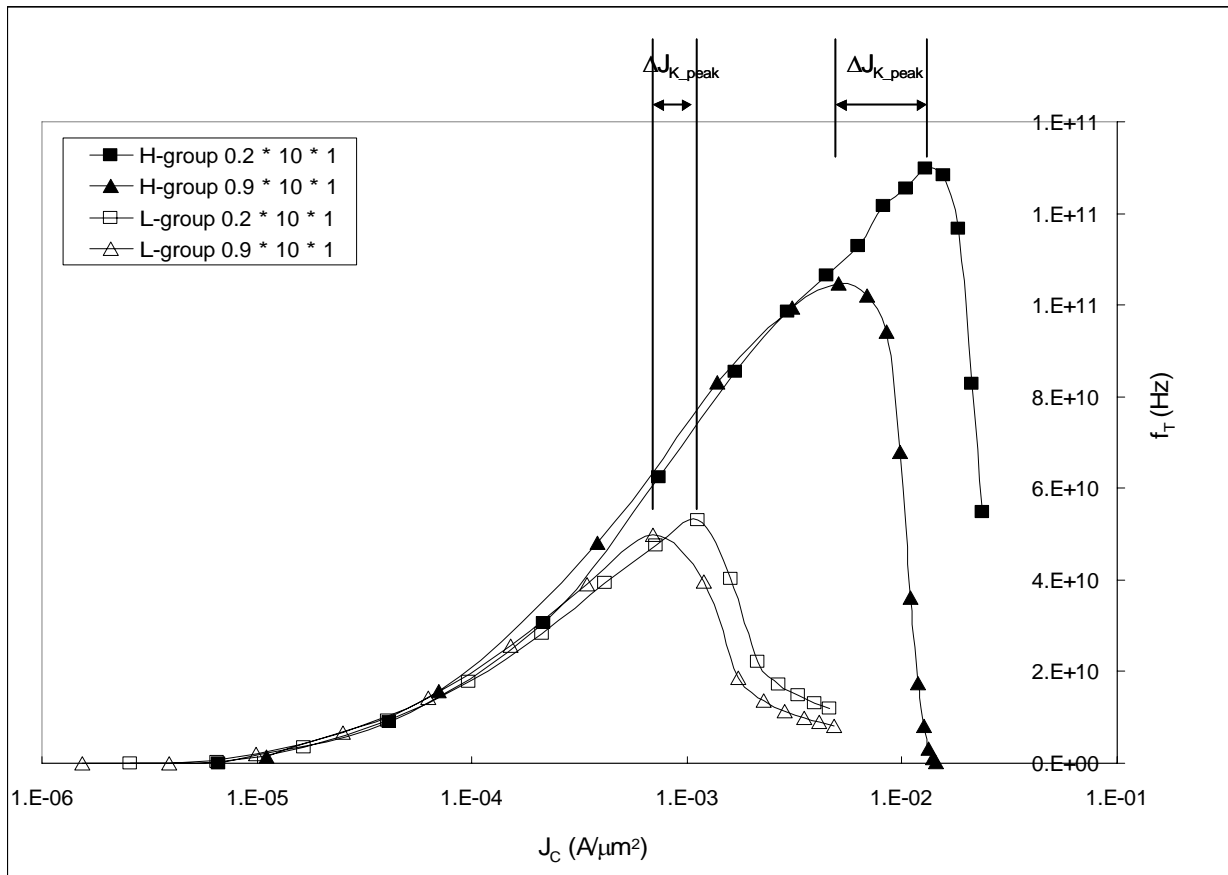
Current spreading in the collector region of L-group device with thinner collector epitaxy layer

Figure 2.3.2 (a)



Current spreading in the collector region of L-group device with thicker collector epitaxy layer

Figure 2.3.2 (b)



f_T - J_C relationships of H and L-group SiGe HBT devices in 0.2 and $0.9 \times 10 \times 1 \mu m^2$

Figure 2.3.3

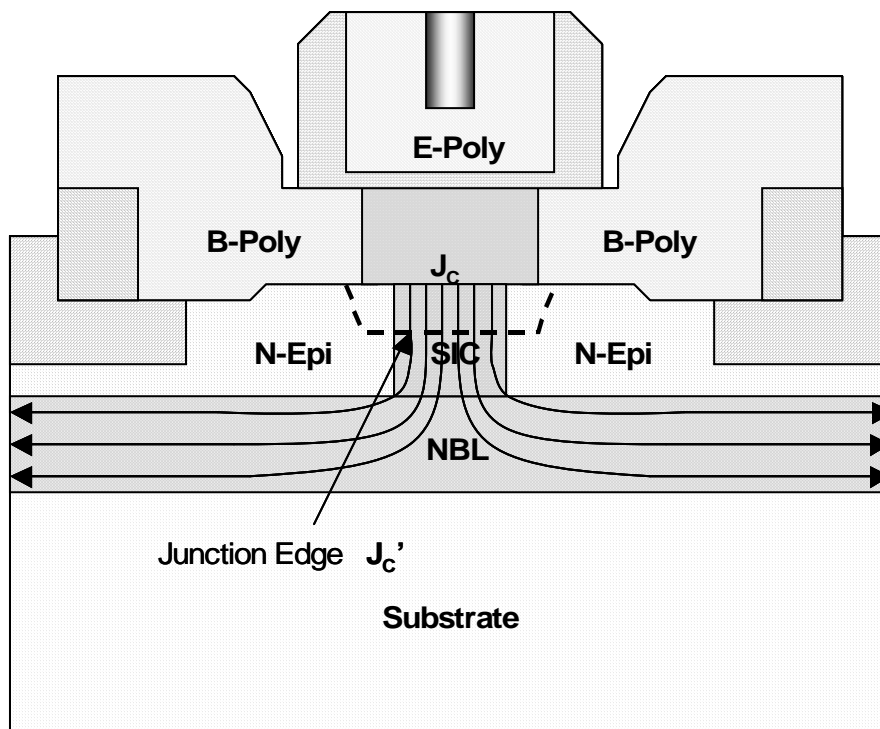
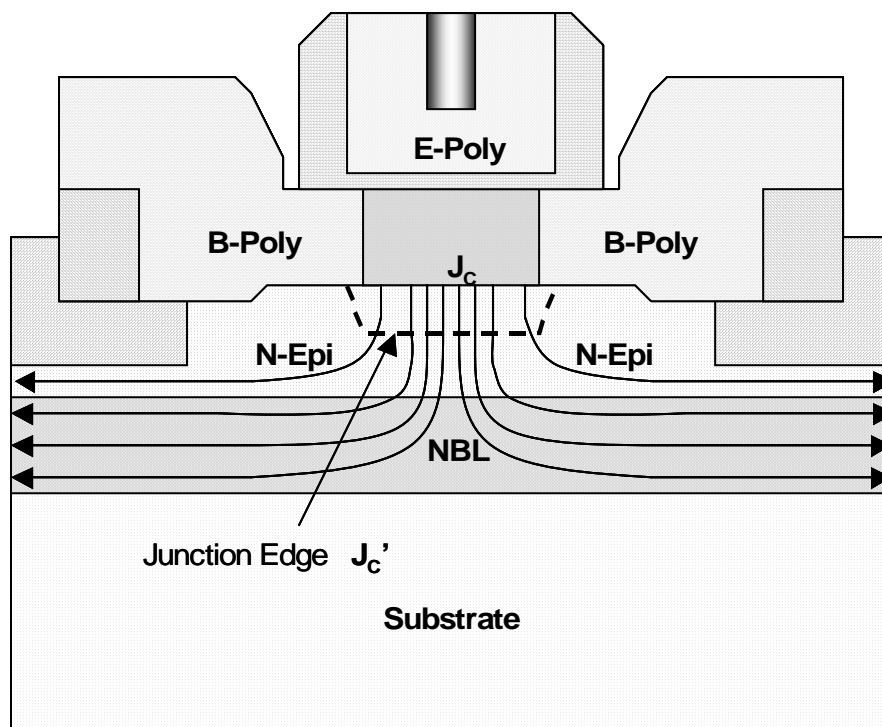


Figure 2.3.4 (a)



Current spreading in the collector region of H-group device with thicker collector epitaxy layer

Figure 2.3.4 (b)